Available online at www.sciencedirect.com
ScienceDirect
Trans. Nonferrous Met. Soc. China 31(2021) 3626−3642
Transactions of Nonferrous Metals Society of China
www.tnmsc.cn

Effect of welding speed on microstructure and mechanical properties of Al−Mg−Mn−Zr−Ti alloy sheet during friction stir welding

Tian DING[1,2], Hong-ge YAN[1,2], Ji-hua CHEN[1,2], Wei-jun XIA[1,2], Bin SU[1,2]

1. School of Materials Science and Engineering, Hunan University, Changsha 410082, China;
2. Hunan Provincial Key Laboratory of Spray Deposition Technology & Application, Hunan University, Changsha 410082, China

Received 27 December 2020; accepted 1 July 2021

Abstract: Effects of welding speed on the microstructure evolution in the stir zone (SZ) and mechanical properties of the friction stir welding (FSW) joints were studied by OM, XRD, SEM, TEM, EBSD and tensile testing. Compared with the base metal (BM), an obviously fine dynamic recrystallization (DRX) microstructure occurs in the SZ and the DRX grain size decreases from 5.6 to 4.4 μm with the increasing of welding speed. Fine DRX microstructure is mainly achieved by continuous dynamic recrystallization (CDRX) mechanism, strain induced boundary migration (SIBM) mechanism and particle stimulated nucleation (PSN) mechanism. Meanwhile, the geometric coalescence and the Burke−Turnbull mechanism are the main DRX grain growth mechanisms. Among all the welding speeds, the joint welded at rotation speed of 1500 r/min and welding speed of 75 mm/min has the greatest tensile properties, i.e. ultimate tensile strength (UTS) of (509±2) MPa, yield strength (YS) of (282±4) MPa, elongation (El) of (23±1)%, and the joint efficiency of 73%.
Key words: friction stir welding; mechanical properties; dynamic recrystallization; nucleation mechanism; grain growth mechanism

1 Introduction

Al−Mg alloys with medium and low Mg content have many advantages, such as good ductility, toughness, weldability and high level of corrosion resistance, but its strength is low [1]. With increasing of Mg content, the strength of the alloys can be improved, but the ductility, weldability and corrosion resistance would decrease. There are many welding methods for Al−Mg alloys, including fusion welding and solid state welding. Conventionally, fusion welding processes have their own limitations with regard to the welding defects such as Mg element evaporation, porosity, solidification cracks, large welding deformation and high level of residual stress [2,3]. Therefore, it is hard to achieve a sound weld with comprehensive mechanical properties via the traditional fusion welding methods, especially for the ductility of the joint. Different from the fusion welding processes, friction stir welding (FSW) is considered as an effective solid-state joining method to weld aluminum alloys [4]. The basic model of FSW is simple. A non-consumable rotating tool with a specially designed pin and shoulder is inserted into the abutting edges of the sheets or the planes to be joined and moved along the line of the joint [5]. Due to the lack of melting during FSW, some defects related to the fusion welding methods can be eliminated, resulting in the higher mechanical properties of the joint than those of the traditional

Corresponding author: Hong-ge YAN, Tel: +86-731-88823554, E-mail: yanhg68@163.com;
Ji-hua CHEN, Tel: +86-731-88823554, E-mail:jihuachen2005@163.com
DOI: 10.1016/S1003-6326(21)65753-9

fusion welding methods.

FSW process experiences a more intense shear deformation and thermal cycle in the stir zone (SZ) that varies as a function of tool geometry, welding speed, and tool rotation speed. Some scholars have investigated the influence of the welding conditions on the microstructure in the SZ and mechanical properties of Al−Mg alloys in recent decades. KUNBHAR et al [6] have pointed out that the microstructural development in the RS (the retreating side) is more obvious than that in the AS (the advancing side). The specimen welded at a lower tool rotation speed exhibits superior mechanical properties, while the welding speed does not affect the tensile properties. HAO et al [7] have found that the SZ shows lower hardness than the BM in the as-rolled sheet, but it just reverses in the as-annealed sheet. The joint efficiency of the as-rolled sheet is 68%, but that of the as-annealed sheet is nearly 100%. Meanwhile, they [8] have also found that increasing the tool rotation speed reduces both ultimate tensile strength (UTS) and yield strength (YS) of the FSW joints, while increasing the welding speed increases both UTS and YS. ZHOU et al [9] have reported that tool rotation speed and welding speed affect the length of the kissing bond. With increasing in the length of the kissing bond, the UTS and elongation increase first and then decrease. The different Mg content and the alloy state are involved with different original microstructures, and thus different microstructures especially dynamic recrystallization (DRX) grain size and precipitate are obtained in the welding area with different welding parameters.

The heat and the shear deformation introduced by the rotation tool during FSW can produce the DRX microstructure in the SZ. Thus, different DRX mechanisms have been studied at present by many scholars. Among these DRX mechanisms, continuous dynamic recrystallization (CDRX), discontinuous dynamic recrystallization (DDRX) and geometric dynamic recrystallization (GDRX) are likely to produce new grains in the SZ. JATA and SEMIATIN [10] have proposed that CDRX is the main grain refinement mechanism during FSW in the high strength Al−Li−Cu alloys firstly. They have thought that the dislocation glide assisted sub-grain rotation model is the main mechanism of CDRX. In this model, dislocation gliding gives rise to a gradual relative rotation of the adjacent sub-grain to the larger angle and finally a DRX grain is formed. This mechanism model has also been confirmed by ETTER et al [11], and they have observed that sub-grains transform into DRX grains by CDRX in the 5251-H14 alloy during the FSW process. However, the DRX mechanism also depends on the original alloy state. ETTER et al [11] have also confirmed that GDRX occurs in the initially annealed microstructure. Meanwhile, the grain size produced by GDRX is more finer than that by CDRX. In recent years, the DDRX nucleation mechanism has been proposed. SAUVAGE et al [12] have reported that DDRX occurs in the FSWed Al−Mg−Sc alloy via the incoherent Al_3Sc precipitates. In addition to the above DRX mechanisms, NADAMMAL et al [13] have found that particle stimulated nucleation (PSN) also could refine the grains in the SZ during the FSW of AA 5083 alloy.

Being the non-heat treatment strengthening aluminum alloys, the Al−Mg alloys exhibit higher strength and lower density with the higher Mg content. It is difficult to obtain the high-quality joints by the traditional fusion welding. However, FSW is an effective method to obtain the joints with excellent mechanical properties. Meanwhile, DRX occurs in the SZ during FSW, which has a great influence on the mechanical properties of the joint. Therefore, it is very important to investigate the microstructure evolution in the SZ of the joint. To date, most studies have been focused on the Al−Mg alloys with low Mg content and the microstructure evolution in the SZ during FSW. However, there is less report on the relationship between the microstructure evolution in the SZ and mechanical properties of the FSWed Al−Mg alloy with high Mg content, especially for the work-hardened state. Therefore, it is worthy of in-depth study. In the present work, the mechanical properties and microstructure evolution in the SZ of FSWed Al−Mg alloys with high Mg content at different welding speeds (v) and a constant rotation speed (w), i.e. w=1500 r/min; v=50, 75, 100, 125 mm/min are investigated. Eventually, the optimum welding speed is determined. Microstructure and texture evolution in the SZ need a further exploration, including the DRX nucleation mechanism and the main grain growth mechanism. Meanwhile, in comparison with base metal (BM), the defect-free joints show high ductility. The reason for the high ductility is worthy of in-depth discussion.

2 Experimental

The as-cold rolled Al−9.2Mg−0.8Mn−0.2Zr−0.15Ti aluminum alloy sheets with the thickness of 2 mm were used for FSW. The as-cast alloys were homogenized at 400 °C for 24 h followed by water quenching. The original thickness was 10 mm, the hot rolling deformation degree was 60% and the cold rolling deformation degree was 50%. The as-cold rolled sheets were butt-welded by FSW perpendicular to the rolling direction (RD). Welds were performed at different welding speeds (v=50, 75, 100, 125 mm/min) under a constant rotational speed of 1500 r/min. The welding tool was fabricated from H13 tool steel and consisted of a shoulder with a diameter of 12 mm and the conical threaded pin, which was 3.6 mm in tip diameter, 2.5 mm in root diameter and anticlockwise rotation, as well as the tool plunge depth maintained to be 0.15 mm. The schematic diagram of FSW is shown in Fig. 1.

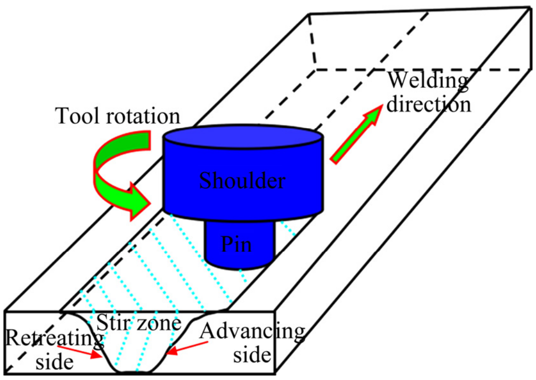

Fig. 1 Schematic diagram of FSW process

Microstructure observations were performed by optical microscopy (OM), electron backscatter diffraction (EBSD) and transmission electron microscopy (TEM). The samples for microstructure observations were etched by Keller's reagent for 60−90 s and then examined by a LeitzMM−6 optical microscopy (OM) and stereoscopy (OLYMPUS DSX510). The residual second phase particles in the BM were observed by scanning electron microscope (SEM, FEI Quanta 200) equipped with Oxford X-ray energy dispersive spectroscopy (EDS). The EBSD analysis was conducted on the SEM (FEI Quanta 200) equipped with the TSL OIM software at the operating potential of 30 kV. TEM observation was performed by using a Titan G2 60-300 transmission electron microscopy. The samples for EBSD and TEM were prepared by electro-polishing and twin-jet electro-polishing in a mixture of 70% CH_3OH + 30% HNO_3 at 15 V and −30 °C. The BM texture measurement was used by X-ray diffraction instrument (Rigaku-Smartlabel) at 40 kV with Cu K_α radiation.

Tensile specimens with the gauge length of 15 mm and the width of 4 mm were cut along the rolling direction for the BM and perpendicular to the welding direction (WD) for the welded samples. Room-temperature tensile tests were conducted at a normal strain rate of 1.1×10^{-3} s^{-1} using an Instron 3369 universal testing machine. The tensile fracture surfaces were observed by SEM (EVO MA10). The microhardness curves were measured on the cross-section perpendicular to the welding direction along the mid-thickness of the sheets using a hardness tester (HVS−1000A) under a load of 200 g for 15 s.

3 Results and discussion

3.1 Microstructure of BM

The microstructures of the BM at different planes are shown in Fig. 2. RD, TD and ND stand for rolling direction, transverse direction and normal direction, respectively. The grains are pancake shaped and elongated in the rolling plane (Fig. 2(a)). The irregular shaped and elongated grains are observed in the transverse cross-sectional plane perpendicular to the rolling direction (Fig. 2(b)). Moreover, the banded structure can be found on the transverse plane parallel to the rolling direction (Fig. 2(c)). SEM image and EDS of the residual second phase are shown in Fig. 3. According to the present work, the main residual second phase is the $Al_6(Fe,Mn)$ phase [14]. Since the $Al_6(Fe,Mn)$ phase has a high melting point higher than 600 °C, it is hard to be dissolved.

The (001), (110) and (111) pole figures of the BM are shown in Fig. 4. From Fig. 4, the texture in the (111) pole figure is higher than that in other two pole figures and the max density is 6.215. In order to determine the specific composition of the texture of the BM, the φ_2=0°, φ_2=45° and φ_2=65° sections of the orientation distribution function (ODF) of the BM are shown in Fig. 5. The ODF sections clearly reveal the strong presence of the deformation texture components. In early literatures, evolution

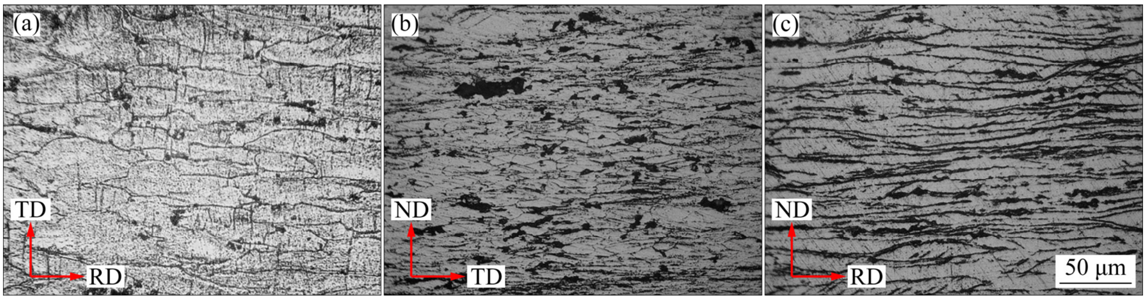

Fig. 2 Optical micrographs of BM in rolling direction (a) and on transverse cross-sectional plane perpendicular to rolling direction (b) and transverse plane parallel to rolling direction (c)

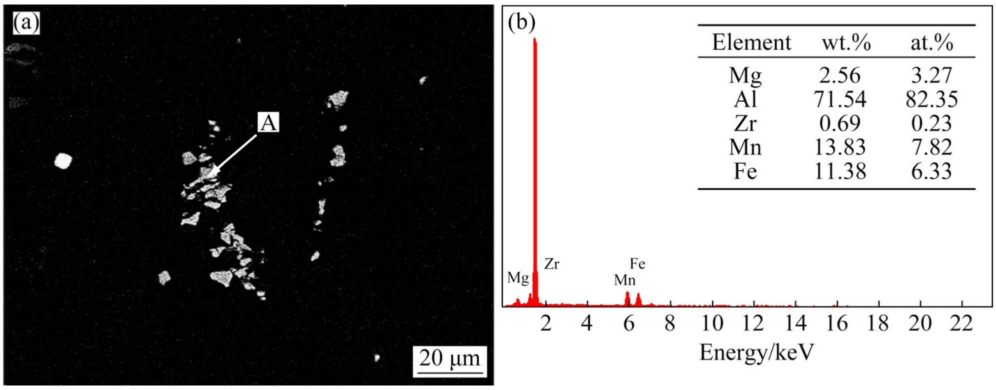

Fig. 3 SEM image (a) and EDS (b) of residual second phase

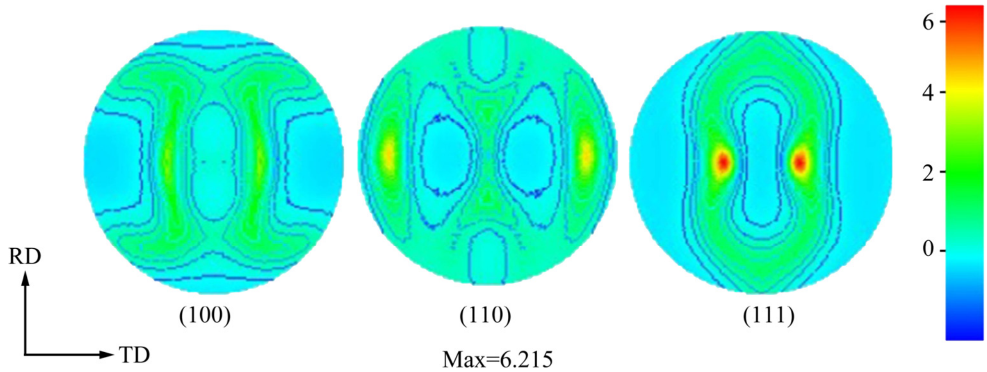

Fig. 4 (001), (110) and (111) pole figures showing texture of BM

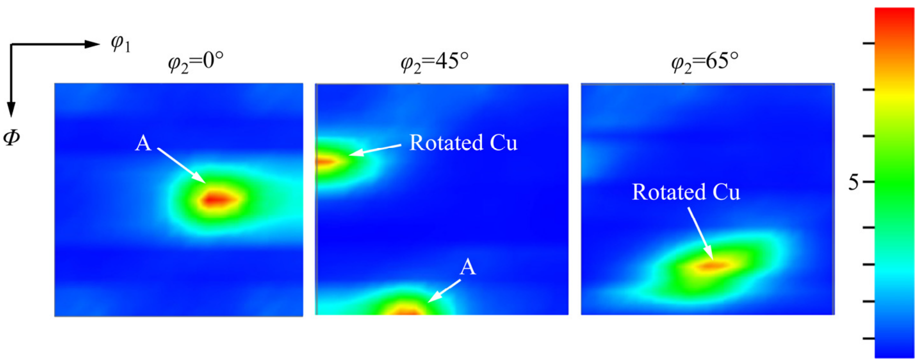

Fig. 5 ODF figures of BM

of texture in face-centered cubic (FCC) materials during thermo-mechanical processing have been researched [15,16]. According to these literatures, we can confirm that rotated Cu ({112}⟨011⟩) and A ({011}⟨111⟩) component textures are observed in the BM, and the A type texture belongs to *α*-fiber texture.

The TEM images of the BM are shown in Fig. 6. A high density of dislocations and small sub-grains are observed in the cold-rolled BM, which is associated with the 50% cold work deformation. As seen from Fig. 6(a), the BM exhibits typical heavily cold-worked characteristic, with a high density of dislocation tangles and dense dislocation walls in the severely deformed grains. From Fig. 6(b), some disc-shaped precipitates and small sub-grains occur in the deformation grains. The disc-shaped precipitate is the $Al_6(Fe,Mn)$ phase, which is the compositional variant of the Al_6Mn phase. The high magnification image of the shallow red rectangle in Fig. 6(b) is shown in Fig. 6(c). The sub-structure consists of nearly equiaxed sub-grains with the mean size of 0.5 μm and a relatively low dislocation density. Dislocation walls are constantly absorbed by sub-grain boundaries to form the large-angle grain boundaries. Meanwhile, the fine sub-grain boundaries can also improve the strength of the alloy.

3.2 Microstructures of welding joints

3.2.1 Cross-sectional macrographs of welding joints

Cross-sectional micrographs of the joints welded with different welding parameters are shown in Fig. 7. All the joints are similar at different welding speeds and thus only one joint is selected to describe the characteristics. As shown in Fig. 7, the welded joint can be roughly divided into four regions, namely BM, heat-affected zone (HAZ), thermo-mechanically affected zone (TMAZ) and SZ. The weld area is wide at the top and narrow at the bottom, showing a basin shape.

The HAZ is closed to the BM and is subjected to sufficient heat during welding without plastic deformation. Heating in the HAZ is high enough to result in the cold-worked recovery and coarsening of precipitates, which is the main cause for the strength reduction in this region. The TMAZ is near the HAZ region and is affected by both thermal cycle and shear force during welding. The SZ is next to the TMAZ, which experiences enough thermal cycle and shear force, thus resulting in completely recrystallized microstructure. A series of concentric ring-like structures are formed in SZ and these concentric rings are called “onion rings”

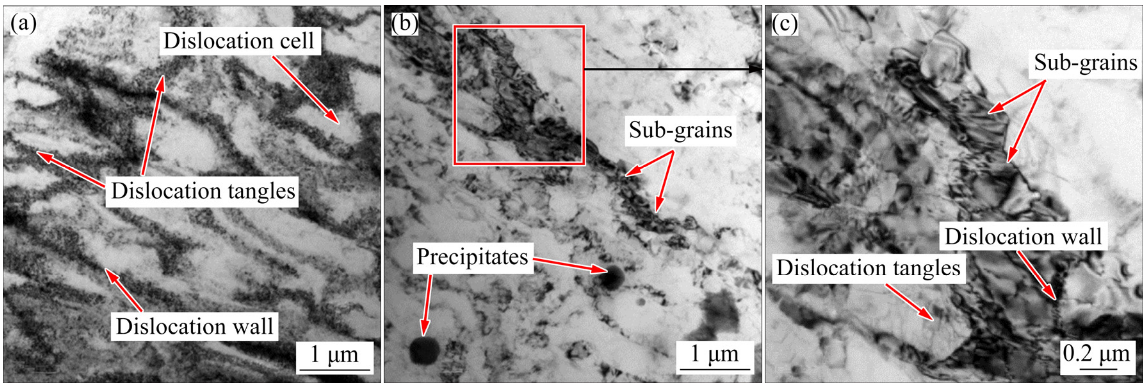

Fig. 6 Bright field TEM images of BM

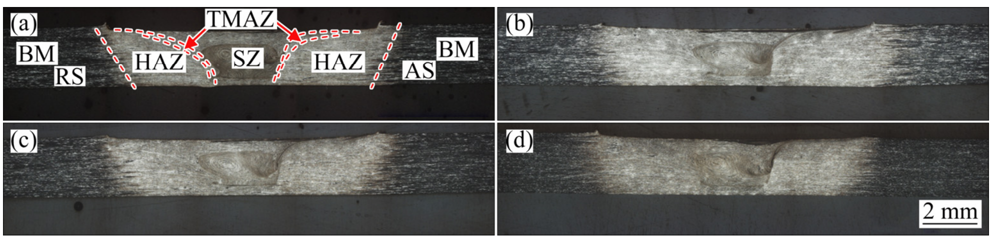

Fig. 7 Cross-sectional micrographs of specimens welded with different welding parameters: (a) 50 mm/min; (b) 75 mm/min; (c) 100 mm/min; (d) 125 mm/min

in many literatures [17,18]. The onion ring is the result of the periodic precipitation of the material layer, which has a certain influence on the mechanical properties of the alloy. There is an interface between the SZ and the TMAZ. The interface where the direction of tool rotation and tool traverse is parallel is known as the "advancing side" (AS), while the opposite direction is called as the "retreating side" (RS). It is noteworthy to mention that, the boundary between the TMAZ and the SZ at the AS is more prominent and sharper than that at the RS, owing to higher heat input of the AS than the RS and different plastic flow states of the metals on both side during the friction process [6,19].

3.2.2 Microstructure of SZ

EBSD images of the SZ at different welding speeds are shown in Fig. 8. It is visible that the equiaxed grains mixed with a few lamellar grains of very low aspect-ratio are obtained in the SZ, which is ascribed to the severe shear deformation and the frictional heat input introduced by the rotation tool during FSW. This process results in many microstructural changes such as dissolution of coarse precipitates, different dynamic recrystallization and recovery mechanisms as well as the texture changes [6,20]. Many scholars have reported that the DRX mechanism in the SZ is CDRX [10,11], which is mainly characterized by the transformation from low-angle grain boundary to large-angle grain boundary by the sub-grain growth and rotation.

As for the SZ, the grain size decreases with increasing of welding speed, which can be ascribed to the larger heat input reduction. The average DRX grain sizes in the SZ are 5.6, 5.1, 4.5 and 4.4 μm, respectively, as shown in Fig. 9. In the FSW process, a semi-quantitative function, the heat input index (H_I) can be expressed [9]:

$$H_\mathrm{I}=w^2/(10^3v) \tag{1}$$

where w is tool rotation speed (r/min), and v is welding speed (mm/min). As shown in Eq. (1), increasing the welding speed leads to the heat input

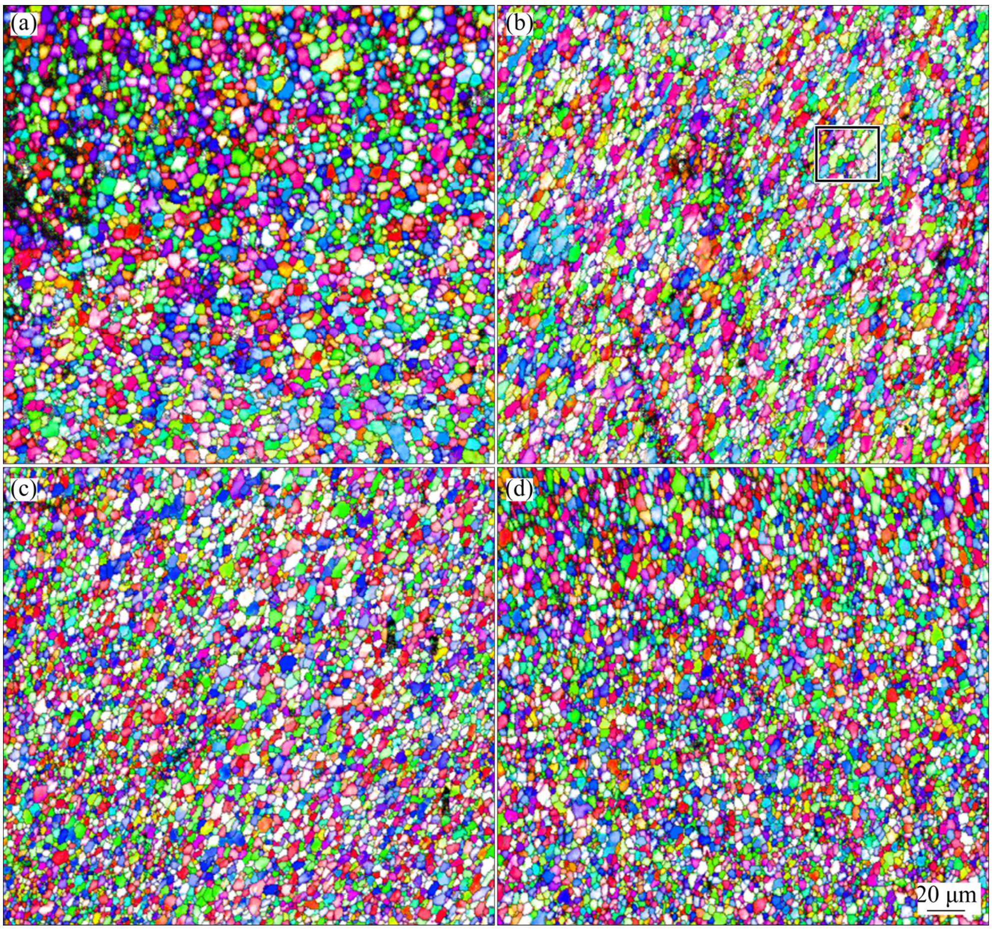

Fig. 8 EBSD maps showing microstructures in SZ at different welding speeds: (a) 50 mm/min; (b) 75 mm/min; (c) 100 mm/min; (d) 125 mm/min

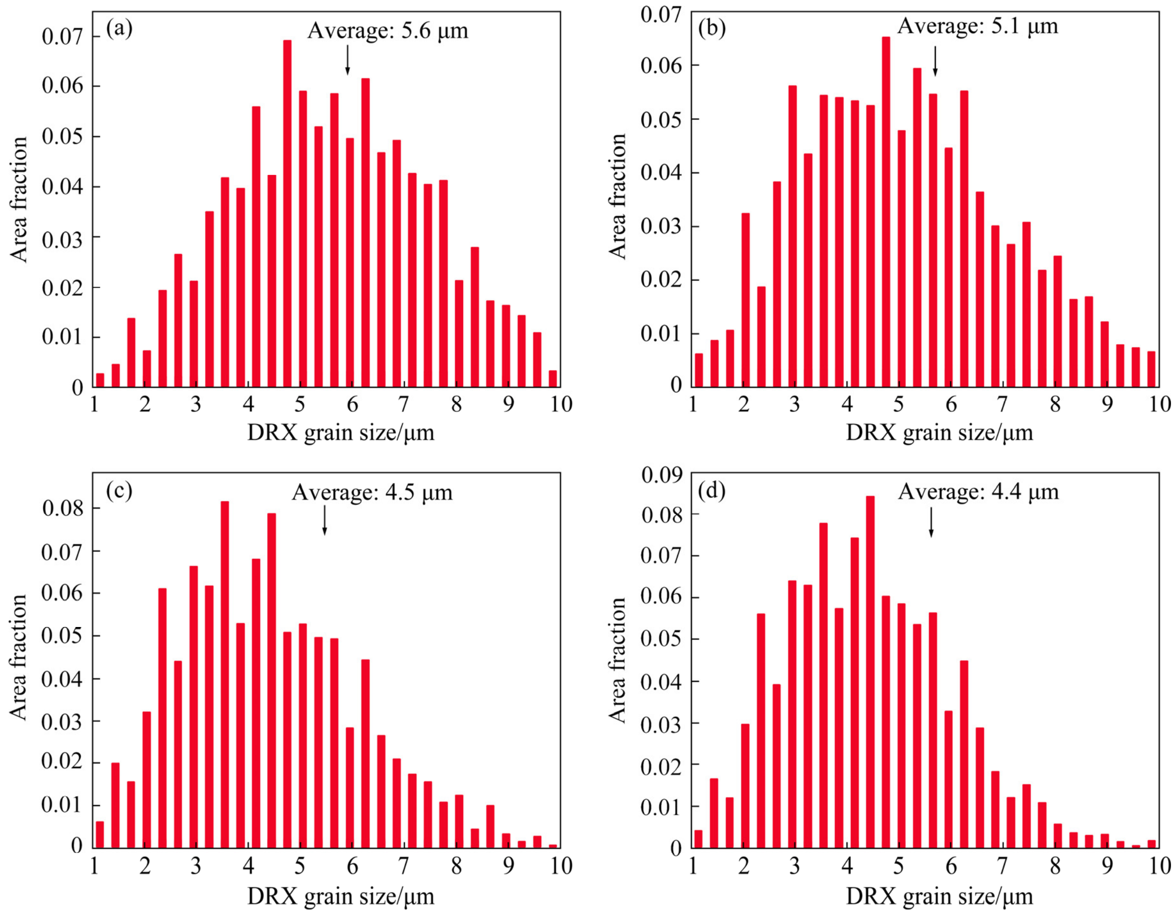

Fig. 9 DRX grain size distributions in SZ at different welding speeds: (a) 50 mm/min; (b) 75 mm/min; (c) 100 mm/min; (d) 125 mm/min

reduction when w is constant. The higher temperature would cause the DRX grain growth. Therefore, the higher welding speed is involved with the reduced heat input, resulting in the finer DRX grain size. The grain size in the SZ accords with the normal distribution. With the welding speeds of 50 and 75 mm/min, the normal distribution pattern is basically symmetrical. However, with the higher welding speed, the number of the grains with the size larger than 6 μm decreases obviously, indicating that the heat input increases at higher welding speed.

The (110) and (111) pole figures showing the texture in the SZ at different welding speeds are shown in Fig. 10. The large heat and intensive shear deformation introduced by the rotation tool into the surrounding materials can produce a variety of microstructures and textures. Many researches on the texture produced during FSW of aluminum alloys exhibit a predominant $\{112\}\langle110\rangle$ texture, corresponding to the B and $\overline{\mathrm{B}}$ components of the ideal shear texture [3,21,22]. For clarity, the positions of the ideal B/$\overline{\mathrm{B}}$ $\{112\}\langle110\rangle$ simple shear texture are shown as white circles in Fig. 10. In comparison with the BM, it can be clearly seen that the texture is very weak and random with the peak intensity being only ~1.6 times. What's more, the texture is very bad-defined and it is hard to precisely interpret in terms of either B/$\overline{\mathrm{B}}$ or other simple shear texture. The main reason for the weak texture in the SZ is that the DRX grains are randomly distributed. MCNELLEY et al [23] have demonstrated that higher volume fractions of dispersed particles may be susceptible to particle simulated nucleation (PSN) of DRX grains, which would lead to a random texture in the SZ. There is no obvious regularity of texture strength at different welding speeds and a little difference in texture strength with each other.

DRX is responsible for the formation of finer grains during FSW. Bright field TEM images of the SZ at rotation speed of 1500 r/min and welding speed of 75 mm/min are shown in Fig. 11. In comparison with the BM, the dislocation density is

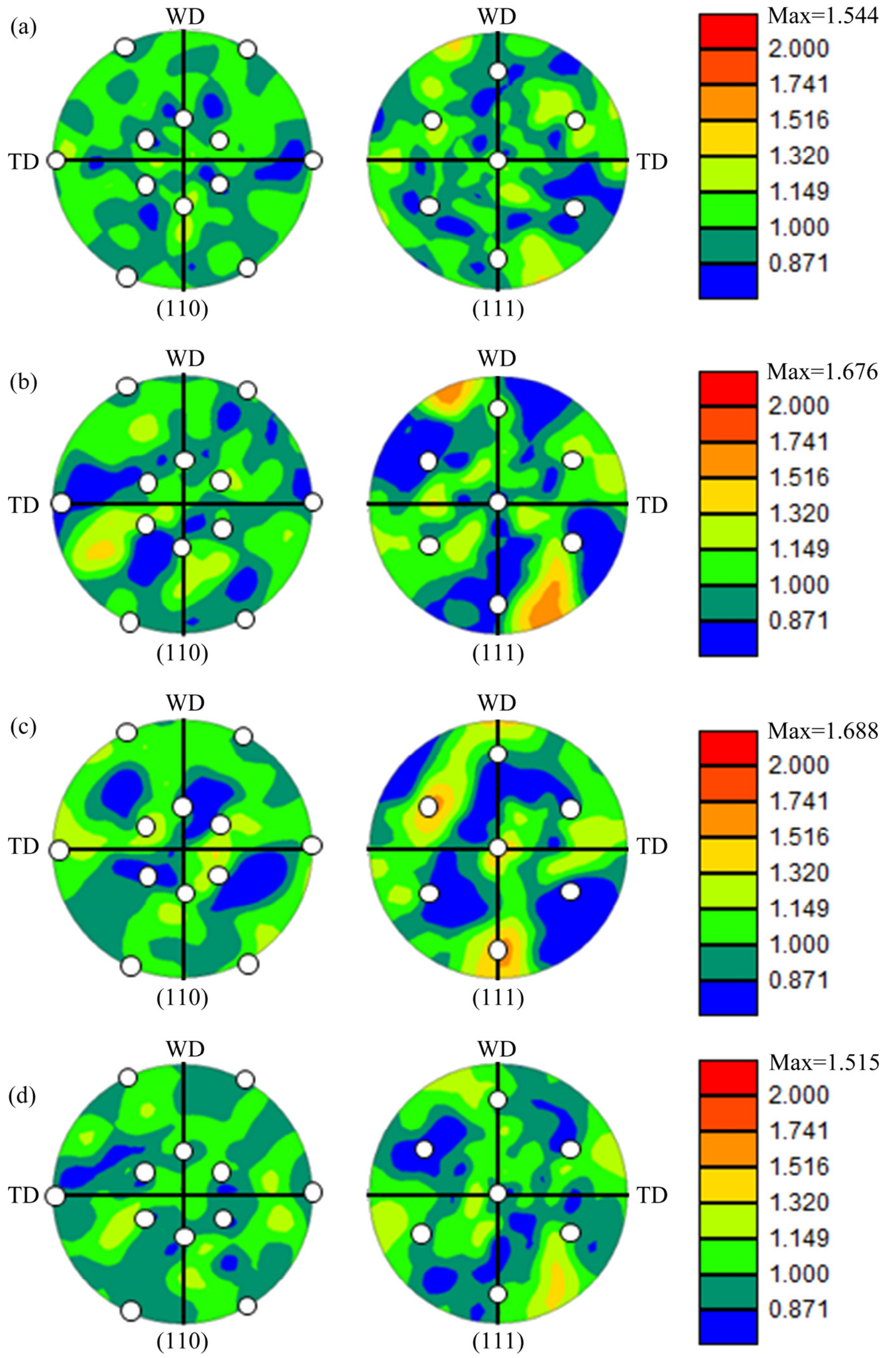

Fig. 10 (110) and (111) pole figures showing texture in SZ at different welding speeds: (a) 50 mm/min; (b) 75 mm/min; (c) 100 mm/min; (d) 125 mm/min

significantly reduced in the SZ (Figs. 11(a−c)), which is ascribed to the DRX microstructure. As shown in Fig. 11(a), the equiaxed fine grains with a low density of dislocations are dominant in the SZ and most grain boundaries are sharp and relatively straight. These grain characteristics indicate that most of the grain boundaries are HAGBs, which is in good agreement with the results obtained by EBSD. Dislocations are generated during FSW and gradually absorbed in the sub-grain boundaries, and then the mis-orientation increases to transform into the low angle grain boundaries (Fig. 11(b)). The sub-grains grow and rotate by repeatedly absorbing the dislocations in the sub-grain boundaries, then forming equiaxed DRX grains with HAGBs [24]. As shown in Fig. 11(c), an ordered dislocation wall alignment occurs inside grain to form new boundaries at the early stage of the sub-grain formation. These sub-grains can eventually grow enough to acquire the HAGBs and thus lead to the nucleation of new grains. According to the above discussion, CDRX is the recrystallization mechanism in the SZ. As shown in Figs. 11(a−c), many fine precipitates occur in the grains. Our recent study shows that the precipitate is the $Al_6(Fe,Mn)$ or Al_6Mn phase [25]. The $Al_6(Fe,Mn)$ phase in the BM is broken and dispersed in the matrix under the action of shear force during FSW.

It is therefore worthwhile to discuss more detailed information on the features of the microstructure evolution. IPF map with grain boundary and two-dimensional grain growth mechanisms are shown in Fig. 12. Figure 12(a) shows a high magnification image of the black rectangle area in Fig. 8(b). The bulging at the grain boundary can be observed at the location marked as "1", indicating the local grain boundary migration. The bulges are formed on the migrated boundaries, which is further surrounded by the low energy dislocation structures in the form of low angle boundary and eventually transforms into fine grains. These features resemble the nucleation stage during strain induced boundary migration (SIBM), indicating that SIBM is possibly another DRX nucleation mechanism during FSW of aluminum alloys. This DRX nucleation mechanism has been reported in the friction stir processed 2219 aluminum alloy [13].

After DRX nucleation, the grains grow under the welding thermal cycle. Grain growth occurs through two major mechanisms, i.e. geometric coalescence [26] and the Burke−Turnbull mechanism [27], which are shown in Figs. 12(b, c), respectively. Some large grains or similarly oriented grains (based on color scheme in an IPF map) are featured in SZ during FSW. Geometric coalescence can easily occur in such situations. Boundary marked as "2" in Fig. 12(a) is between two grains in different orientations (depicted by different colors). Boundary between these two grains is a low angle boundary and these two grains can coalesce together as a single grain. In Burke−

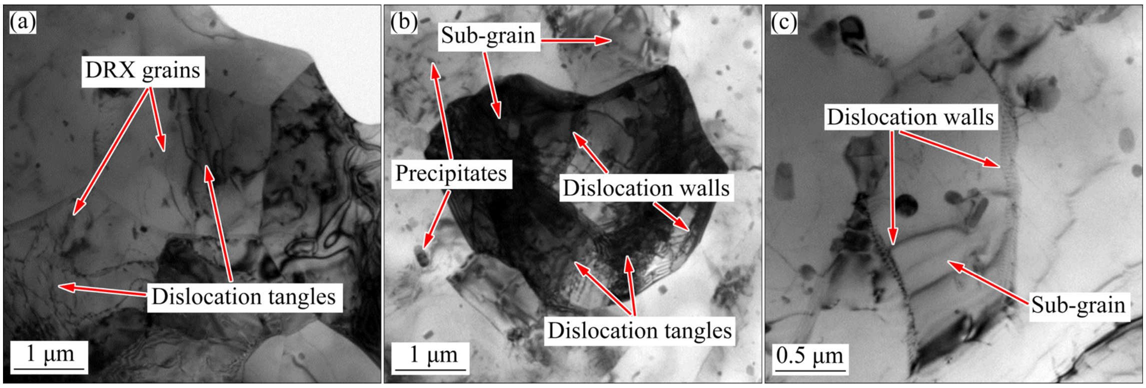

Fig. 11 Bright field TEM images of SZ at rotation speed of 1500 r/min and welding speed of 75 mm/min

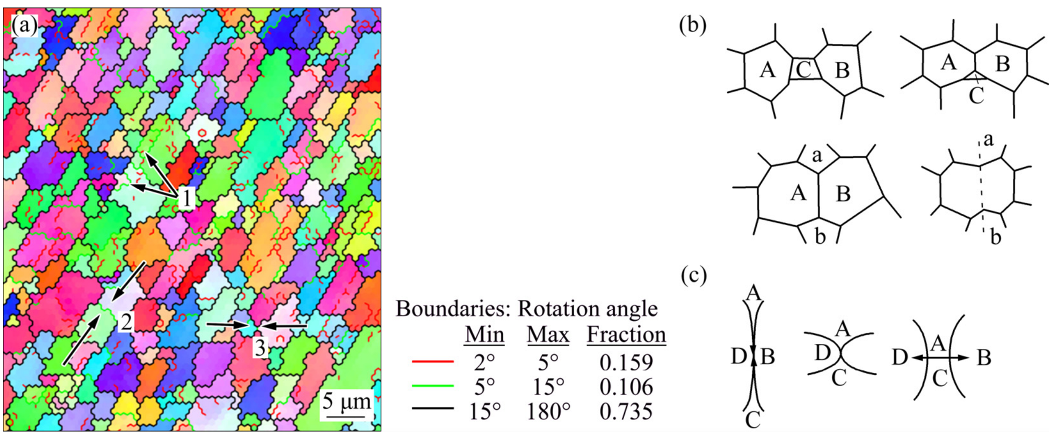

Fig. 12 IPF map with grain boundary and two-dimensional grain growth mechanisms: (a) IPF map; (b) Geometrical coalescence [26]; (c) Burke−Turnbull mechanism [27]

Turnbull mechanism, triple junctions are formed easily at the grain boundaries during FSW with the stable dihedral angle configuration of 120°. This process would continue until a stable grain orientation occurs. Such observation is found in Fig. 12(a), marked as "3". The grain growth mechanisms marked by "2" and "3" are the final states of the two major mechanisms.

Phase distributions in the SZ at different welding speeds are shown in Fig. 13. Severe shear force and frictional heat input during friction stir welding would lead to the dissolution of coarse precipitates and re-precipitation associated with the weld thermal cycle. According to Eq. (1), the heat input decreases with increasing of welding speed. Therefore, the number of precipitates in SZ decreases. Meanwhile, the Mg content in α(Al) also increases. It has been reported that the peak temperature can reach above 450 °C in the SZ during FSW of Al alloys [28]. The β-Al_3Mg_2 phase would precipitate from α(Al) in the temperature range from 175 to 250 °C [29]. Thus, the β-Al_3Mg_2 phase would precipitate from α(Al) in the SZ during FSW due to the high peak temperature and sever shear deformation. As a solution strengthening alloy, the formation of the β-Al_3Mg_2 phase would decrease the Mg content in α(Al), reducing the mechanical properties. According to Section 3.1,

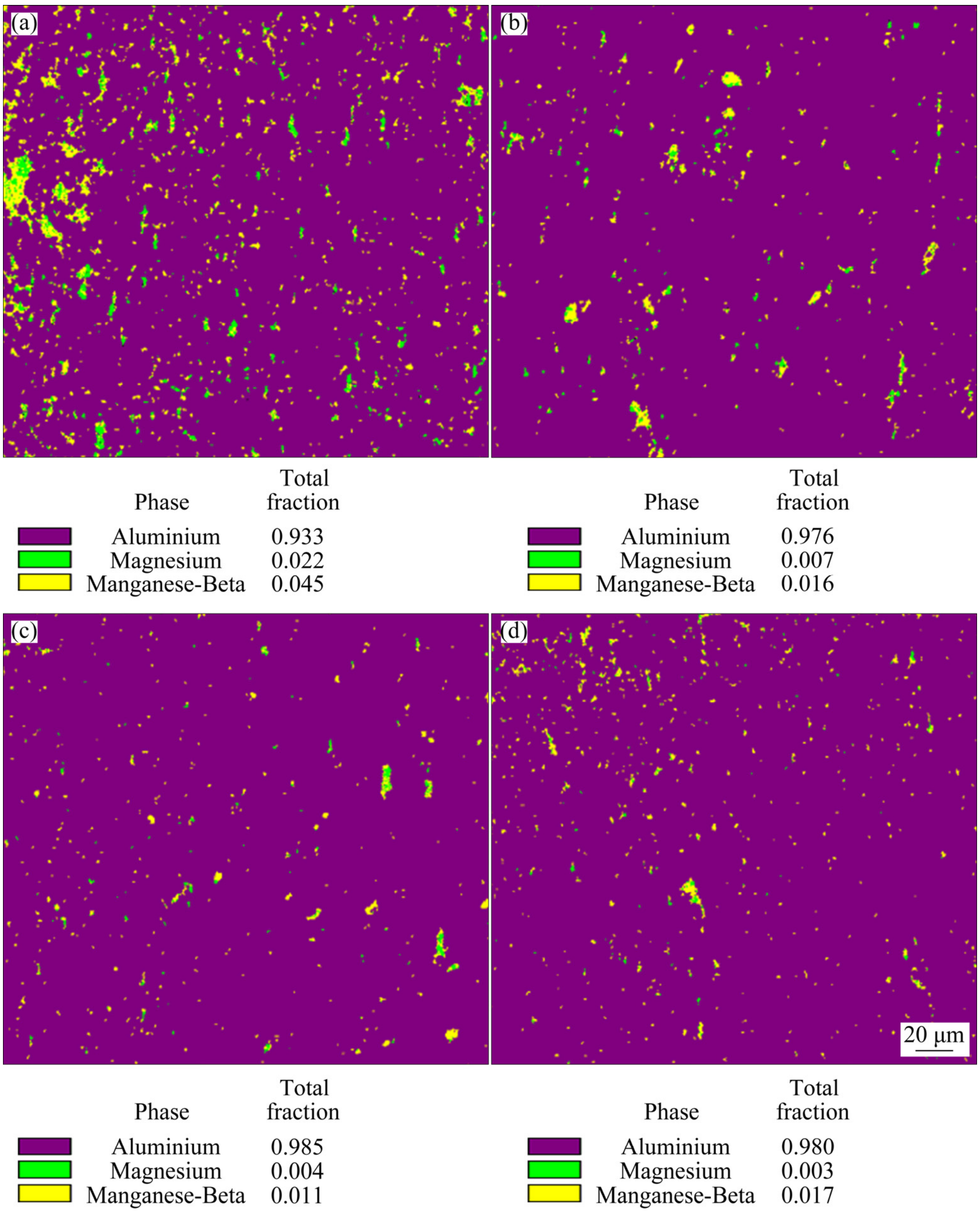

Fig. 13 Phase distributions in SZ at different welding speeds: (a) 50 mm/min; (b) 75 mm/min; (c) 100 mm/min; (d) 125 mm/min

BM contains the $Al_6(Fe,Mn)$ phase. During the FSW process, these residual second phases would be broken and dispersed in SZ under the action of severe shear force. As seen from Fig. 13, it is clear that the SZ microstructure after FSW retains many broken second phases (>1 μm). Thus, some very fine DRX grains are observed in the SZ due to the PSN. PSN is one important recrystallization mechanism, which has been confirmed by the relevant studies [13,23].

3.3 Mechanical properties

Tensile properties of the BM and the welded specimens at different welding speeds are shown in Fig. 14. The specific experimental values are summarized in Table 1. Firstly, all the joints exhibit lower UTS and YS than the BM. Secondly, as far as the rotating speed of 1500 r/min is concerned, UTS, YS and elongation of the joint welded at 75 mm/min are 509 MPa, 282 MPa and 23%, respectively, which are higher than those at other welding speeds. Thirdly, all the joints exhibit higher ductility than the BM.

The studied alloy is a non-heat-treatable Al−Mg alloy and its strength is primarily due to the high solute concentration and the associated work hardening. This alloy contains 9.2 wt.% Mg and experiences 50% cold work deformation. As shown in Figs. 6(a−c), a high density dislocations and sub-grain boundaries are observed in the grains, both of which are beneficial to the strength improvement since they act as obstacles to dislocation motion. Therefore, the effect of dislocation strengthening is more obvious. In addition, a great number of Mg atoms are dissolved into the matrix and act as obstacles to dislocation motion. Furthermore, more Mg atoms would diffuse close to the mobile dislocations and inhibit their motion during tensile loading [30]. Thus, the high strength of BM can be ascribed to the dislocation strengthening and the solution strengthening associated with the addition of Mg element.

During the welding process, the high-strain-rate deformation and the high temperature can bring about large microstructure changes, which affect the mechanical properties. Since DRX grains are formed in the SZ, essential material softening is observed in the SZ. This effect is ascribed to the elimination of the work hardening effect due to the occurrence of DRX during FSW. In other words, the relatively low UTS and YS of the joint are mainly attributed to the reduction of dislocation density in the weld zone. Thus, all the joints exhibit significant reduction in UTS and YS in comparison with the BM.

However, the joints exhibit notably higher

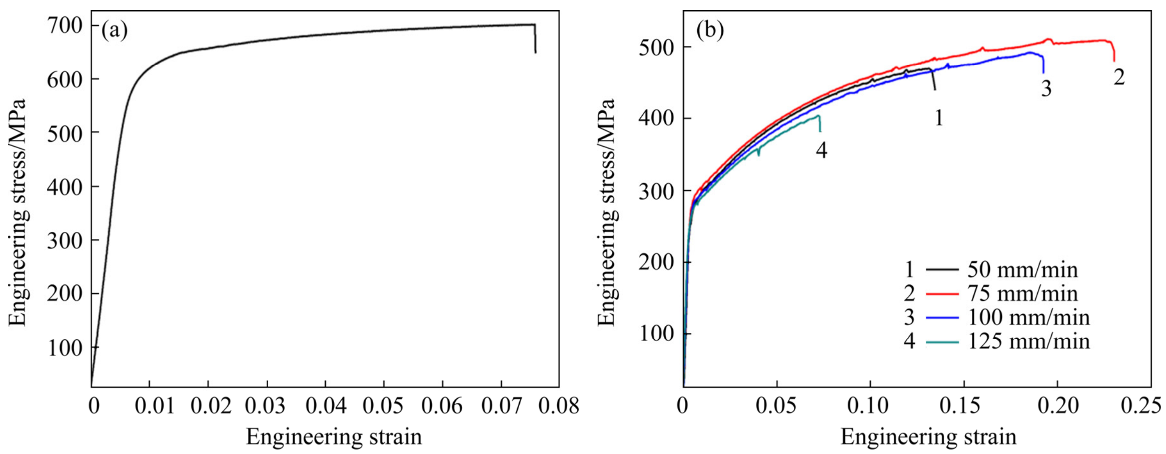

Fig. 14 Engineering stress−strain curves of BM (a) and FSW joints (b) at different welding speeds

Table 1 Transverse tensile properties of BM and FSW joints at room temperature

Part	Welding speed/(mm·min^{-1})	UTS/MPa	YS/MPa	Elongation/%	Joint efficiency/%
BM	−	695±3	597±4	7±1	−
FSW joint	50	470±4	273±3	14±1	68
	75	509±2	282±4	23±1	73
	100	492±1	278±1	17±2	70
	125	417±13	267±2	6±2	60

ductility, except for the samples welded at 1500 r/min and 125 mm/min. The ductility is affected by work hardening and strain rate sensitivity. The high values of these parameters can delay the onset of localized deformation under the tensile stress, thus improving the ductility. The low ductility of the BM is attributed to the lack of work hardening caused by their inability to accumulate dislocations during the tensile testing because of the saturation of dislocations. Therefore, the basic idea to improve the ductility is to regain the work hardening, i.e. dislocation accumulation capability. The fine grains with HAGBs are beneficial to improving the ductility, as reported in some literatures [31,32], because the HAGBs can improve the work hardening by effectively enhancing the dislocation accumulation capability. Obviously, the fine grains with very low dislocation density in the FSW joint (Figs. 11(a−c)) due to DRX result in the enhanced work hardening capacity, where the dislocations can be effectively accumulated in the tensile testing. Meanwhile, a great number of HAGBs in the FSW joint compared to the BM can be effective in blocking the movement of dislocations and thus result in more dislocations to tangle and accumulate near the boundaries. In addition, FSW can produce a more homogenous microstructure and the stress redistribution during the tensile testing can delay the strain localization [33], thus achieving a considerable elongation before failure. What's more, FSW with the high friction heat results in grain coarsening, thus leading to an increase in the dislocation storage capacity. Therefore, the ductility of the FSW joints can be improved. Moreover, the weak texture in the SZ could help to improve the ductility of the FSW joints. XIAO et al [34] have reported that the change from strong deformation texture to the weak recrystallization texture is beneficial to enhancing the ductility, as the fine grains with random orientation are good for the uniform distribution of stress, and thus the higher tensile strain can be achieved during tensile deformation. The weak and random texture feature of the FSWed alloys at different welding speeds also helps to improve the ductility of the FSW joints.

With the higher welding speed, the tensile properties increase at first and then gradually decrease. Although the grain size in the SZ welded at 125 mm/min is smaller than the others, the tensile properties are the lowest. Microstructures at the bottom of SZ on the AS side at different welding speeds are shown in Fig. 15. As shown in Fig. 15, the void defect only occurs in the AS at 125 mm/min. The channel defect or void is a common defect in FSW, which is the result of the improper selection of welding parameters. The higher welding speed leads to the insufficient heat input in the weld and the tool has a shorter time to plasticize and move the alloy around the pin, resulting in the insufficient plastic deformation under the welding condition [35]. Recently, there has been a consensus that the inappropriate material flow is the main reason for the defect formation during FSW. A number of factors have been identified to contribute to the formation of voids or channel defects, including inadequate welding pressure, high welding speed and slow rotation speed as well as inadequate control of the joint gap [36]. When welding at a high welding speed or a slow rotation speed, the material receives less work per unit of the welding length, i.e. fewer tool rotations per millimeter [37]. Under such conditions, the plasticized material cannot reach a sufficiently high temperature, resulting in the lower volume of the plasticized material. In the process of FSW, the stirring pin constantly transfers the plasticized material from the advancing side to the retreating side. Due to the poor fluidity of the plasticized material, the material on the advancing side cannot be filled in time by the plasticized material from the retreating side, resulting in the less amount of material in this area and thus finally forming voids or channel defects. Of course, when the rotation speed and the welding speed are high in the FSW process, abnormal stirring of the material occurs and finally the channel defects are formed. It is considered that the abnormal stirring is caused by the temperature difference between the upper part near the surface and the bottom part [38]. From the above discussion, the improper selection of the process parameters results in insufficient plasticization of the material and the imbalance in material movement around the stirring pin, and thus voids or channel defects are formed [35]. This welding defect is the most important cause for the dramatic decrease in both strength and ductility of the joint welded at welding speed of 125 mm/min.

With the lower welding speed, the heat input

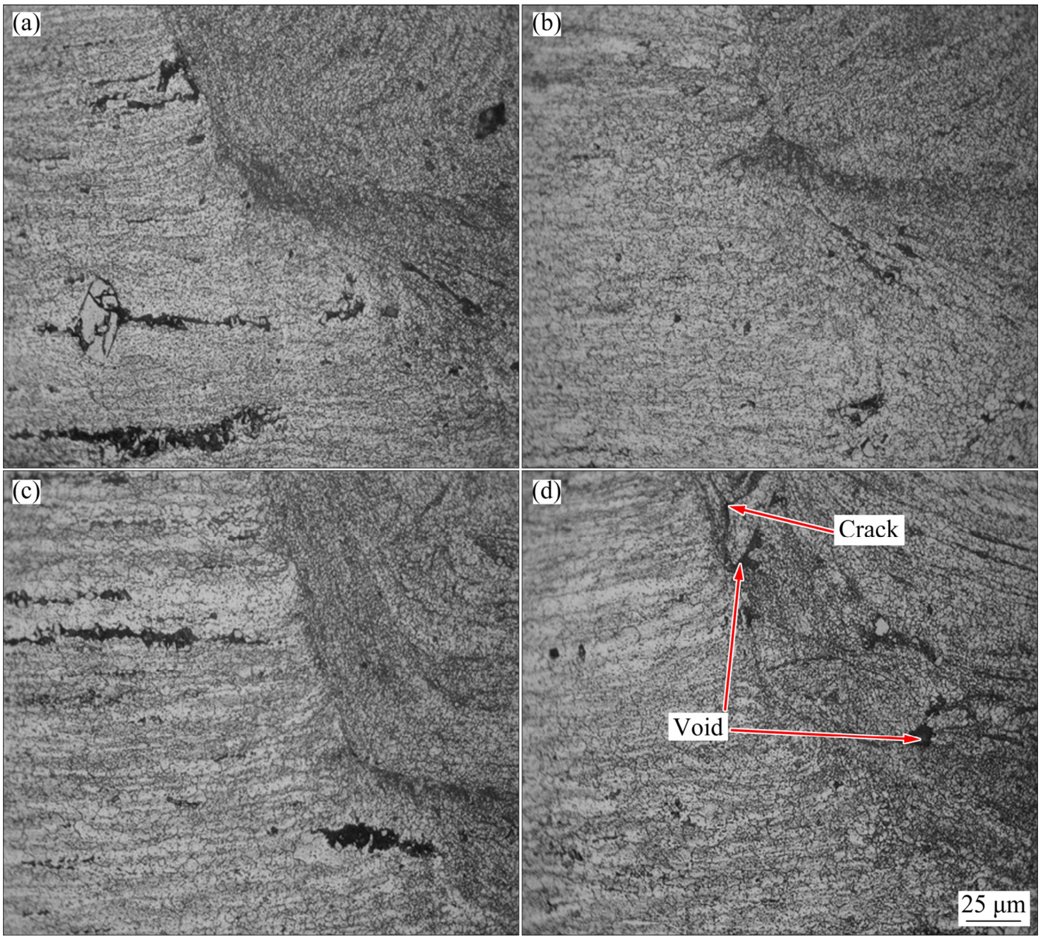

Fig. 15 Microstructures at bottom of SZ on AS side at different welding speeds: (a) 50 mm/min; (b) 75 mm/min; (c) 100 mm/min; (d) 125 mm/min

increases. The higher heat input leads to the grain coarsening and the dissolution of the second phase β-Al_3Mg_2 in the SZ and thus reduces the tensile properties [39]. It is believed that the variation in tensile properties of the FSW joints with the welding speed is associated with the microstructure evolution. In addition to the grain size, the characteristics such as the number and the size of the precipitates as well as 'onion rings' also affect the mechanical properties of the alloy [40,41]. The best mechanical properties are obtained with the welding speed of 75 mm/min, showing that the microstructure can be optimized by the proper match of the rotational speed and the welding speed. The lower welding speed can change the grain size and the second phase, while the higher welding speed results in the defects. Hence, an optimum welding speed is essential to generate adequate frictional heat since it can generate the defect-free joint by the sufficient straining of the plasticized material with the fine DRX grains.

3.4 Microhardness

The microhardness curves of the FSW joints along the mid thickness of the transverse section at different welding speeds are shown in Fig. 16. The hardness curves are "W" shaped and asymmetric, due to the asymmetric temperature in the welded zone since the SZ attains a higher temperature on the AS than on the RS [42]. Moreover, all the weld joints exhibit the remarkably reduced hardness in the welded zone compared to the BM, which is ascribed to the annealing softening and recrystallization in the welded zone [43]. During the FSW, the SZ experiences the intense plastic deformation and thermal exposure with the peak temperatures up to (0.6−0.95)T_M, and thus the significant annealing softening and recrystallization occur [44]. Furthermore, at a constant rotation rate of 1500 r/min, the higher welding speed brings about the lower peak temperature and results in the narrower softening zone. In addition, the hardness

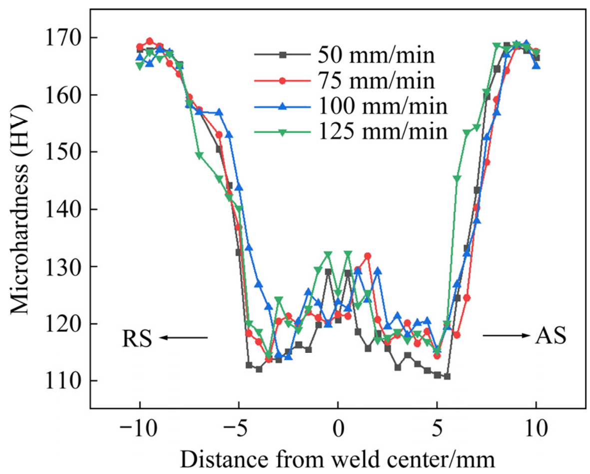

Fig. 16 Microhardness curves at different welding speeds

of the SZ increases from HV 127 to 133 with the welding speed increasing from 50 to 125 mm/min, owing to the smaller grain size. Therefore, the hardness of the SZ in all of the weld joints is higher than that of the AS and RS.

3.5 Tensile fracture

The SEM tensile fracture images of the BM and the FSW joints at different welding speeds are shown in Fig. 17. The size and the number of dimples and tear edges are different for the FSW samples.

As seen from Fig. 17(a), some cracks and large cleavage facets are detected on the fracture surfaces of the BM, indicating that the brittle fracture is the main facture mode. As seen from Figs. 17(b−e), more dimples occur on the fracture surfaces of FSW samples compared to the BM, indicating that the ductile fracture is the main fracture mode. More large-size dimples are detected in FSW samples at the welding speeds of 75 and 100 mm/min, which is in good consistency with the relatively high ductility. According to the previous study, the second phase in the fracture is mainly the $Al_6(Fe,Mn)$ phase. Cracks and voids are formed in the joints welded at welding speed of 125 mm/min, which is in good consistency with the low ductility.

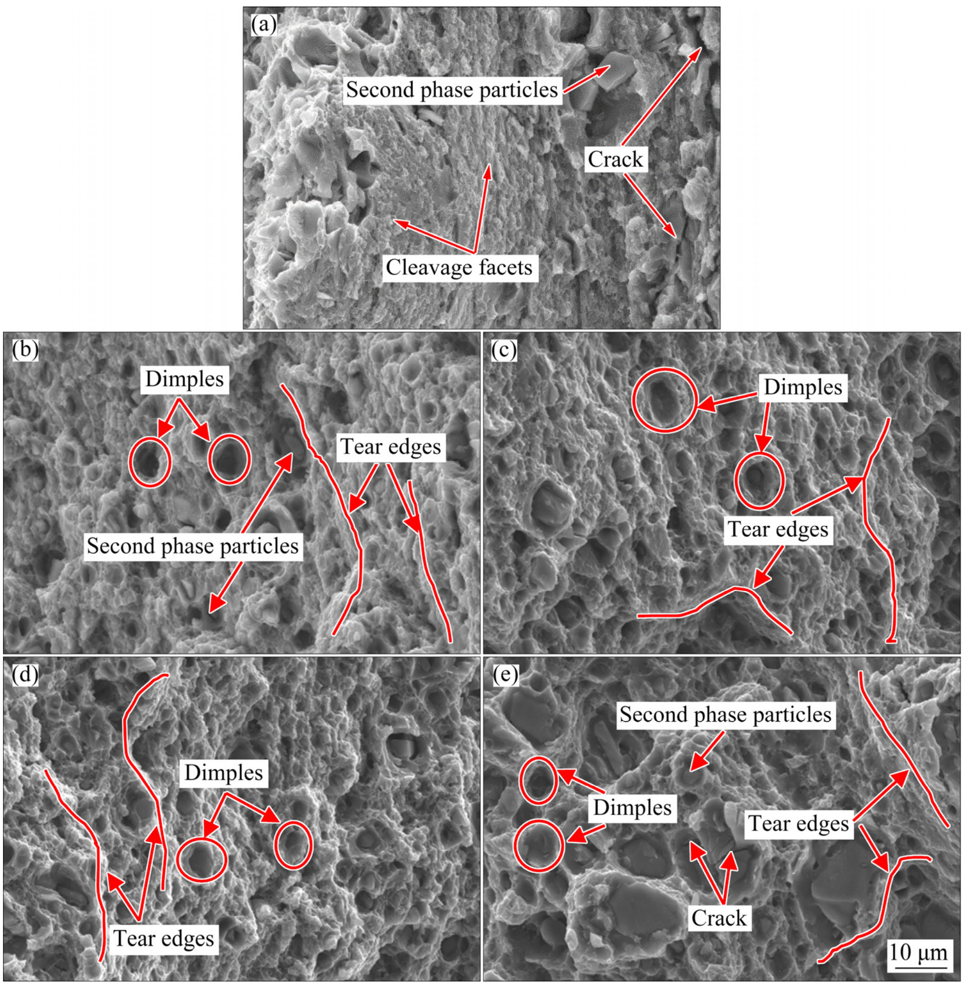

Fig. 17 SEM tensile fracture images of BM and FSW joints: (a) BM; (b) 50 mm/min; (c) 75 mm/min; (d) 100 mm/min; (e) 125 mm/min

4 Conclusions

(1) FSW produce fine equiaxed grains through CDRX, SIBM and PSN mechanisms. The grain size in SZ decreases from 5.6 to 4.4 μm with increasing of welding speed owing to the heat input decreasing.

(2) With the higher welding speed, the tensile properties increase at first and then gradually decrease. Higher heat input at low welding speed leads to grain growth and void defect produced at high welding speed. Among all the weld parameters, the defect-free joint welded at the rotation speed of 1500 r/min and the welding speed of 75 mm/min has the greatest tensile properties, i.e. ultimate tensile strength (UTS) of (509±2) MPa, yield strength (YS) of (282±4) MPa, elongation (El) of (23±1)%, and the joint efficiency of 73%.

(3) The higher ductility of the FSW joints compared to the BM is attributed to the fine DRX grains with high-angle grain boundaries (HAGBs) and a more homogenous SZ microstructure, as well as the weak and random texture.

Acknowledgments

The authors would like to express their sincere gratitude to the Sawing Engineering Research Center of Hunan Province (China) for the assistance in macrostructure observation of the joints.

References

[1] SHE Xin-wei, JIANG Xian-quan, WANG Pu-quan, TANG Bin-bin, CHEN Kang, LIU Yu-jie, CAO Wei-nan. Relationship between microstructure and mechanical properties of 5083 aluminum alloy thick plate [J]. Transactions of Nonferrous Metals Society of China, 2020, 30: 1780−1789.

[2] HE Zhen-bo, PENG Yong-yi, YIN Zhi-min, LEI Xue-feng. Comparison of FSW and TIG welded joints in Al−Mg−Mn−Sc−Zr alloy plates [J]. Transactions of Nonferrous Metals Society of China, 2011, 21: 1685−1691.

[3] KHAN N Z, KHAN Z A, SIDDIQUEE A N, AL-AHMARI A M, ABIDI M H. Analysis of defects in clean fabrication process of friction stir welding [J]. Transactions of Nonferrous Metals Society of China, 2017, 27: 1507−1516.

[4] SHARMA N, KHAN Z A, SI SIDDIQUEE A N. Friction stir welding of aluminum to copper−An overview [J]. Transactions of Nonferrous Metals Society of China, 2017, 27: 2113−2136.

[5] WEN Q, LI W Y, WANG W B, WANG F F, GAO Y J, PATEL V. Experimental and numerical investigations of bonding interface behavior in stationary shoulder friction stir lap welding [J]. Journal of Materials Science and Technology, 2019, 35: 192−200.

[6] KUNBHAR N T, SAHOO S K, SAMAJDAR I, DEY G K, BHANUMURTHY K. Microstructure and microtextural studies of friction stir welded aluminum alloy 5052 [J]. Materials and Design, 2011, 32(3): 1657−1666.

[7] HAO H L, NI D R, ZHANG Z, WANG D, XIAO B L, MA Z Y. Microstructure and mechanical properties of Al−Mg−Er sheets jointed by friction stir welding [J]. Materials and Design, 2013, 52: 706−712.

[8] HAO H L, NI D R, HUANG H, WANG D, XIAO B L, NIE Z R, MA Z Y. Effect of welding parameters on microstructure and mechanical properties of friction stir welded Al−Mg−Er [J]. Materials and Science Engineering A, 2013, 559: 889−896.

[9] ZHOU N, SONG D F, QI W J, LI X H, ZOU J, ATTALLAH M M. Influence of the kissing bond on the mechanical properties and fracture behavior of AA5083-H112 friction stir welds [J]. Materials and Science Engineering A, 2018, 719: 12−20.

[10] JATA K V, SEMIATIN S L. Continuous dynamic recrystallization during friction stir welding of high strength aluminum alloys [J]. Scripta Materials, 2000, 43(8): 743−749.

[11] ETTER A L, BAUDIN T, FREDJ N, PENELLE P. Recrystallization mechanisms in 5251 H14 and 5251 O aluminum friction stir welds [J]. Materials Science and Engineering A, 2007, 445−446: 94−99.

[12] SAUVAGE X, DEDE A, MUNOA A C, HUNEAU B. Precipitate stability and recrystallization in the weld nuggets of friction stir welded Al−Mg−Si and Al−Mg−Sc alloys [J]. Materials Science and Engineering A, 2008, 491: 364−371.

[13] NADAMMAL N, KAILAS S V, SZPUNAR J, SUWAS S. Restoration mechanisms during the friction stir processing of aluminum alloys [J]. Metallurgical and Materials Transaction A, 2015, 46: 2823−2828.

[14] LI Xin-yu, XIA Wei-jun, YAN Hong-ge, CHEN Ji-hua, SU Bin, SONG Min, LI Zhen-zhen, LI Ying-li. Dynamic recrystallization behaviors of high Mg alloyed Al−Mg alloys during high strain rate rolling deformation [J]. Materials Science and Engineering A, 2019, 753: 59−69.

[15] HIRSCH J, LUCKE K, HATHERLY M. Mechanism of deformation and development of rolling textures in polycrystalline F.C.C. metals −III. The influence of slip inhomogeneities and twinning [J]. Acta Metallurgical, 1988, 36(11): 2905−2927.

[16] JAMAATI R, TOROGHINEJAD M R. Effect of stacking fault energy on deformation texture development of nanostructured materials produced by the ARB process [J]. Materials Science and Engineering A, 2014, 598: 263−276.

[17] TONGNE A, JAHAZI M, FEULVARCH E, DESRAYAUD C. Banded structures in friction stir welded Al alloys [J]. Journal of Materials Processing Technology, 2015, 221: 269−278.

[18] SUTTON M A, YANG Bang-cheng, REYNOLDS A P, YAN Jun-hui. Banded microstructure in 2024-T351 and 2524-T351 aluminum friction stir welds: Part II. Mechanical

characterization [J]. Materials Science and Engineering A, 2004, 364: 66−74.

[19] CHEN Shu-jun, LI Xiao-xu, JIANG Xiao-qing, YUAN Tao, HU Ya-zhou. The effect of microstructure on the mechanical properties of friction stir welded 5A06 Al alloy [J]. Materials Science and Engineering A, 2018, 735: 382−393.

[20] YAZDIPOUR A, SHAFIEI A, DEHGHANI K. Modeling the microstructural evolution and effect of cooling rate on the nanograins formed during the friction stir processing of Al5083 [J]. Materials Science and Engineering A, 2009, 527: 192−197.

[21] MALOPHEYEV S, KULITSKIY V, MIRONOV S, ZHEMCHUZHNIKOVA D, KAIBYSHEV R. Friction-stir welding of an Al−Mg−Sc−Zr alloy in as-fabricated and work-hardened conditions [J]. Materials Science and Engineering A, 2014, 600: 159−170.

[22] MALOPHEYEV S, MIRONOV S, KULITSKIY V, KAIBYSHEV R. Friction-stir welding of ultra-fine grained sheets of Al−Mg−Sc−Zr alloy [J]. Materials Science and Engineering A, 2015, 624: 132−139.

[23] MCNELLEY T R, SWAMINATHAN S, SU Jiang-qing. Recrystallization mechanisms during friction stir welding/ processing of aluminum alloys [J]. Scripta Materials, 2008, 58(5): 349−354.

[24] SU Jian-qing, NELSON T W, STERLING C J. Microstructure evolution during FSW/FSP of high strength aluminum alloys [J]. Materials Science and Engineering A, 2005, 405: 277−286.

[25] LI Ying-li, YAN Hong-ge, CHEN Ji-hua, XIA Wei-jun, SU Bin, DING Tian, LI Xin-yu. Influences of welding speed on microstructure and mechanical properties of friction stir welded Al−Mg alloy with high Mg content [J]. Materials Research Express, 2020, 7(7): 076506.

[26] NIELSEN J P. Recrystallization, grain growth and texture [M]//ASM Seminar Series. American Society for Metals. Metals Park, Ohio, 1966: 141−164.

[27] BURKE J E, TURNBULL D. Recrystallization and growth [J]. Progress in Metal Physics, 1952, 3: 220−292.

[28] KIM D G, BADARINARYAN H, KIM J H, KIM C, OKAMOTO K, WAGONER R H, CHUNG K. Numerical simulation of friction stir butt welding process for AA5083-H18 sheets [J]. European Journal of Mechanics−A Solid, 2010, 29(2): 204−215.

[29] WANG B B, CHEN F F, LIU F, WANG W G, XUE P, MA Z Y. Enhanced mechanical properties of friction stir welded 5083Al-H19 joints with additional water cooling [J]. Journal of Materials Science & Technology, 2017, 33(9): 1009−1014.

[30] LEE B H, KIM S H, PARK J H, KIM H W. Role of Mg in simultaneously improving the strength and ductility of Al−Mg alloys [J]. Materials Science and Engineering A, 2016, 657: 115−122.

[31] PENG Yong-yi, YIN Zhi-min, NIE Bo, ZHONG Li. Effect of minor Sc and Zr on superplasticity of Al−Mg−Mn alloys [J]. Transactions of Nonferrous Metals Society of China, 2007, 17: 744−750.

[32] NING Jiang-li, JIANG Da-ming, FAN Xi-gang, LAI Zhong-hong, MENG Qing-chang, WANG Dian-liang. Mechanical properties and microstructure of Al−Mg−Mn−Zr alloy processed by equal channel angular pressing at elevated temperature [J]. Materials Characterization, 2008, 59(3): 306−311.

[33] CHEN Y, LIU C Y, ZHANG B, MA Z Y, ZHOU W B, JIANG H J, HUANG H F, WEI L L. Effects of friction stir processing and minor Sc addition on the microstructure, mechanical properties, and damping capacity of 7055 Al alloy [J]. Materials Characterization, 2018, 135: 25−31.

[34] XIAO Han, LU Zhen, ZHANG Kai-feng, JIANG Shao-song, SHI Cheng-cheng. Achieving outstanding combination of strength and ductility of the Al−Mg−Li alloy by cold rolling combined with electropulsing assisted treatment [J]. Materials and Design, 2020, 186: 108279.

[35] DEHGHANI M, AMADEH A, MOUSAVI S A A A. Investigations on the effects of friction stir welding parameters on intermetallic and defect formation in joining aluminum alloy to mild steel [J]. Materials and Design, 2013, 49: 433−441.

[36] THREADHILL P L, LEONARD A J, SHERCLIFF H R, WITHERS P J. Friction stir welding of aluminum alloys [J]. International Materials Reviews, 2009, 54(2): 49−93.

[37] SATO Y S, URATA M, KOKAWA H. Parameters controlling microstructure and hardness during friction-stir welding of precipitation-hardenable aluminum alloy 6063 [J]. Metallurgical and Materials Transaction A, 2002, 33: 625−635.

[38] KIM Y G, FUJII H, TSUMURA T, KOMAZAKI T, NAKATA K. Three defect types in friction stir welding of aluminum die casting alloy [J]. Materials Science and Engineering A, 2006, 415: 250−254.

[39] MOSHWAN R, YUSOF F, HASSAN M A, RAHMAT S M. Effect of tool rotational speed on force generation, microstructure and mechanical properties of friction stir welded Al−Mg−Cr−Mn (AA 5052-O) alloy [J]. Materials and Design, 2015, 66: 118−128.

[40] MALOPHEYEV S, MIRONOV S, KULITSKIY V, KAIBYSHEV R. Friction-stir welding of ultra-fine grained sheets of Al−Mg−Sc−Zr alloy [J]. Materials Science and Engineering A, 2015, 624: 132−139.

[41] FONDA R W, BINGERT J F. Precipitation and grain refinement in a 2195 Al friction stir weld [J]. Metallurgical and Materials Transaction A, 2006, 37: 3593−3604.

[42] WADE W, REYNOLDS A P. Friction stir weld nugget temperature asymmetry [J]. Science and Technology of Welding and Joint, 2010, 5(1): 64−69.

[43] WEN Quan, LI Wen-ya, PATEL V, BERGMANN L, KLUSEMANN B, SANTOS J F. Assessing the bonding interface characteristics and mechanical properties of bobbin tool friction stir welded dissimilar aluminum alloy joints [J]. Acta Metallurgica Sinica, 2021, 34: 125−134.

[44] PATEL V, LI Wen-ya, WANG Guo-qing, WANG Fei-fan, VAIRIS A, NIU Peng-liang. Friction stir welding of dissimilar aluminum alloy combinations: State-of-the-art [J]. Metals, 2019, 9(3): 270−289.

搅拌摩擦焊接过程中焊接速度对 Al−Mg−Mn−Zr−Ti 合金板材显微组织及力学性能的影响

丁 天[1,2]，严红革[1,2]，陈吉华[1,2]，夏伟军[1,2]，苏 斌[1,2]

1. 湖南大学 材料科学与工程学院，长沙 410082；
2. 湖南大学 湖南省喷射沉积技术与应用重点实验室，长沙 410082

摘 要：利用 OM、XRD、SEM、TEM、EBSD 和拉伸测试研究搅拌摩擦焊接过程中焊接速度对焊合区的显微组织以及接头力学性能的影响。与母材相比，焊合区中产生明显的细小动态再结晶显微组织，并且随着焊速的增加，动态再结晶晶粒尺寸从 5.6 μm 降低至 4.4 μm。细小动态再结晶显微组织主要是通过连续动态再结晶、应变诱导晶界迁移以及粒子激发形核机制获得。与此同时，几何合并和伯克−特恩布尔机制是主要的动态再结晶晶粒生长机制。采用搅拌针转速 1500 r/min 和焊接速度 75 mm/min 时，接头具有最佳的拉伸性能，即抗拉强度为(509±2) MPa、屈服强度为(282±4) MPa、塑性为(23±1)%以及接头效率为 73%。

关键词：搅拌摩擦焊接；力学性能；动态再结晶；形核机制；晶粒生长机制

(Edited by Bing YANG)